

Direct imaging of orbitals in quantum materials

Hasan Yavas,^{1,2,*} Martin Sundermann,^{1,3} Kai Chen,^{3,†} Andrea Amorese,^{1,3}

Andrea Severing,^{1,3} Hlynur Gretarsson,^{1,2} Maurits W. Haverkort,⁴ and Liu Hao Tjeng¹

¹Max Planck Institute for Chemical Physics of Solids, Nöthnitzer Straße 40, 01187 Dresden, Germany

²PETRA III, Deutsches Elektronen-Synchrotron (DESY), Notkestraße 85, 22607 Hamburg, Germany

³Institute of Physics II, University of Cologne, Zùlpicher Straße 77, 50937 Cologne, Germany

⁴Institute for Theoretical Physics, Heidelberg University, Philosophenweg 19, 69120 Heidelberg, Germany

The spectacular physical properties of quantum materials based on transition metal, rare earth, and actinide elements continue to challenge our comprehension of solid state physics and chemistry. The electronic states of these materials are dominated by the d and f wave functions intertwined with the strong band formation of the solid. In order to estimate which wave functions contribute to the ground state formation, we have had to rely, until now, on theoretical calculations combined with spectroscopy. Here we show that s -core-level non-resonant inelastic x-ray scattering (s -NIXS) can directly image the active orbital in real space, without the necessity of any modeling. The power and accuracy of this new technique is shown using the text-book example, $x^2-y^2/3z^2-r^2$ orbital of the Ni^{2+} ion in NiO single crystal.

The search for new materials with novel properties is commonly focused on materials containing transition metal, rare-earth, and/or actinide elements. The presence of the atomic-like d or f wave functions provide a fruitful playground to generate novel phenomena [1–5]. The intricate interplay of band formation with the local electron correlation and atomic multiplet effects leads to phases that are nearly isoenergetic, making materials' properties highly tunable by doping, temperature, pressure, or magnetic field. Understanding the behavior of the d and f electrons is essential for designing and controlling novel quantum materials. Therefore, identifying the d or f wave functions that actively participate in the formation of the ground state is crucial. So far, these wave functions have been mostly deduced from optical, x-ray and neutron spectroscopy methods in which spectra must be analyzed and interpreted using theory or modeling. This, however, is also a challenge in and of itself since *ab-initio* calculations hit their limits due to the many-body nature of the problem. Here, we have established an experimental method that circumvents the need for involved analysis, and instead, provides the information as measured. With this technique, we can make a direct image of the active orbital and determine what the atomic-like object looks like in a real solid.

The spectral intensity of the dipole-allowed $s \rightarrow p$ transition depends on the orientation of the electric field polarization vector of the photon relative to the orientation of the p orbital [6]. Since the s orbital is spherically symmetric, sweeping the polarization vector over all angles yields an angular intensity distribution that directly maps the shape and orientation of the p orbital hole. Yet, material research requires knowledge of d and/or f orbital shapes. As the $s \rightarrow d$ or $s \rightarrow f$ transitions are dipole forbidden, it has been challenging to develop an experimental method that has non vanishing matrix elements *beyond the dipole limit*. However, the relatively new experimental method of non-resonant inelastic x-ray

scattering (NIXS), available due to modern synchrotron facilities with high brilliance, has offered new potential.

The interaction of light with matter is given by two terms: a term proportional to the scalar product of the electron momentum operator \vec{p} and the photon vector potential \vec{A} , and a term proportional to the vector potential \vec{A} squared. When photon energy matches an atomic resonance, the $\vec{p} \cdot \vec{A}$ term dominates; off-resonance, the interaction is governed by the \vec{A}^2 term. Focusing on this last term using NIXS, the double differential cross-section $\frac{d^2\sigma}{d\Omega d\omega}$ becomes proportional to the dynamical structure factor $S(\vec{q}, \omega)$ [7] which contains the material-specific information we are seeking:

$$S(\vec{q}, \omega) = \sum_f |\langle f | e^{i\vec{q} \cdot \vec{r}} | i \rangle|^2 \delta(\hbar\omega_i - \hbar\omega_f - \hbar\omega),$$

where $|i\rangle$ and $|f\rangle$ denote the (many-body) initial and final states, $\vec{q} = \vec{k}_i - \vec{k}_f$ the transferred momentum, $\hbar\omega = \hbar\omega_i - \hbar\omega_f$ the transferred energy, and $\vec{k}_{i,f}$ and $\hbar\omega_{i,f}$ the momentum and energy of the incoming and scattered photons, respectively.

Beyond-dipole matrix elements appear in the scattering cross-section when expanding the transition operator $e^{i\vec{q} \cdot \vec{r}}$ to the k^{th} order, whereby k denotes the *multipole order of the scattering cross-section* [7–16]. The so-called triangular condition and parity rule restrict the number of multipoles to $|l_f - l_i| \leq k \leq l_f + l_i$ and $|l_i + l_f + k| = \text{even}$ for a $l_i \rightarrow l_f$ transition (respective orbital momenta of initial and final state). This implies that for a $d \rightarrow f$ transition, only dipole ($k = 1$), octopole ($k = 3$), and triakontadipole ($k = 5$) scattering orders occur, and for $s \rightarrow d$ - a dipole-forbidden transition - only the quadrupole transition with $k = 2$ contributes to $S(\vec{q}, \omega)$. For small momentum transfers $|\vec{q}|$, the NIXS spectra very much resemble dipole-allowed x-ray absorption spectroscopy (XAS). In other words, the NIXS $2p/3p \rightarrow 3d$ excitations in transition metal compounds [8, 10] or the $3d/4d \rightarrow 4f/5f$ and

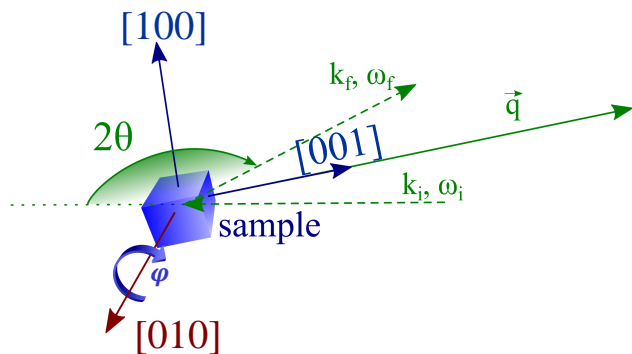


FIG. 1: The scattering geometry is defined by the incoming and the scattered beam, k_i, ω_i and k_f, ω_f , respectively (dashed green arrows). This geometry, which outlines the scattering triangle, remains fixed throughout the measurements. The single crystal sample (blue) is rotated around an axis perpendicular to the scattering plane (maroon) by an angle φ , and for each φ an inelastic spectrum is collected. Here, $\varphi = 0$ refers to $\vec{q} \parallel [001]$ (specular geometry).

$5d \rightarrow 5f$ excitations in rare earth and actinide materials [9, 10] exhibit line shapes that are very similar to the ones obtained from XAS [17–21]. The only difference is that in NIXS, the direction of the momentum transfer \hat{q} ($\vec{q}/|\vec{q}|$) provides the information that is obtained from the electrical vector polarization in XAS. However, for large $|\vec{q}|$, for the same metal ion, the $p \rightarrow d$ or $d \rightarrow f$ transitions yield a different spectral distribution with additional features that cannot be seen in a dipole-based XAS experiment [7–16, 22, 23]. Moreover, the dipole-forbidden $s \rightarrow d$ or $s \rightarrow f$ transitions (quadrupolar or octopolar, respectively) now have non-vanishing matrix elements, and consequently are allowed and become visible.

The novelty of our approach is to exploit these s -core-level transitions involving our search for a new method to determine - quantitatively and model free - the local valence orbitals that make up the electronic structure of d and f containing quantum materials. We investigated the $s \rightarrow d$ transition in an inelastic x-ray scattering experiment (s -NIXS) at large momentum transfers $|\vec{q}|$ and map the quadrupolar scattering intensity as a function of the direction of the momentum transfer \hat{q} relative to the crystal lattice. We used a single crystal of NiO, an antiferromagnetic insulator [24], with a Ni d^8 configuration as a model system; and the large momentum transfers were guaranteed by high scattering angles and hard x-rays.

In our experimental setup as illustrated in Fig. 1, $S(\vec{q}, \omega)$ of the NiO sample was recorded as a function of the sample angle φ , here defined as the angle between the fixed momentum transfer vector \vec{q} and the NiO surface normal (see Methods). Fig. 2 shows a compilation of NIXS spectra measured for many different sample angles. The spectra show the $M_{2,3}$ edge ($3p \rightarrow 3d$) of nickel at around 70 eV and, most impor-

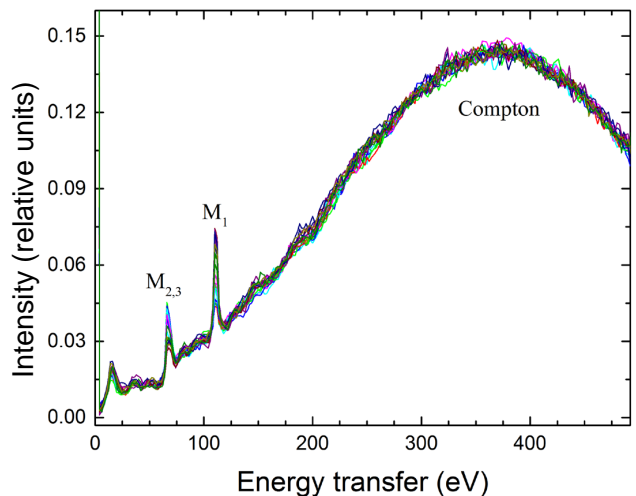


FIG. 2: Experimental NIXS spectra of NiO. Compilation of spectra, which were collected for a variety of crystal rotations φ with respect to the geometrically fixed momentum transfer vector \vec{q} . The graph shows all the spectra. The Compton profile peaks at approximately 350 eV and is used for data normalization. The dipole-allowed Ni $M_{2,3}$ ($3p \rightarrow 3d$) edge at around 70 eV energy transfer and the dipole-forbidden Ni M_1 ($3s \rightarrow 3d$) excitations at around 110 eV can be clearly observed. The data exhibit an excellent signal to background (Compton) ratio in the energy range of the Ni edges, rendering NIXS as a high-contrast experiment.

tantly, the dipole-forbidden M_1 ($3s \rightarrow 3d$) excitations at around 110 eV, overlaid on the broad Compton profile. The signal to background ratio is excellent in the energy range of the M_1 edge. A close-up of this edge and its directional dependence on \vec{q} along $\vec{q} \parallel [001]$ and $\vec{q} \parallel [100]$ are displayed in Fig. 3 a, and for \vec{q} along $\vec{q} \parallel [001]$ and $\vec{q} \parallel [110]$ in Fig. 3 b and c. In the close-up plots, the Compton profile has been subtracted using a simple linear background (see Methods).

To quantitatively analyze the $3s \rightarrow 3d$ transition's directional dependence, we determined the integrated intensity of each spectrum in Fig. 3 and placed it on a polar plot as displayed in (Fig. 4). Panel (a) shows the data points for \vec{q} sweeping in the $[001]$ – $[100]$ plane (orange), and panel (b) for \vec{q} in the $[001]$ – $[110]$ plane (green). They fall accurately on top of the orbital shapes which denote 'cuts' through the $[001]$ – $[100]$ (orange) and $[001]$ – $[110]$ (green) planes of the three-dimensional orbital hole state of the Ni high-spin $3d^8$ configuration in octahedral coordination, namely the ${}^3A_2 3d(x^2 - y^2)3d(3z^2 - r^2)$ as shown in Fig. 4 (c). This means that, for the first time, we have generated a purely experimental method that can directly visualize the fundamental atomic-like quantum mechanical objects in solids. The information that we have obtained is extremely detailed; for example, we can see nicely and clearly see the small lobes of the $3d(3z^2 - r^2)$. Here we note that we have used two

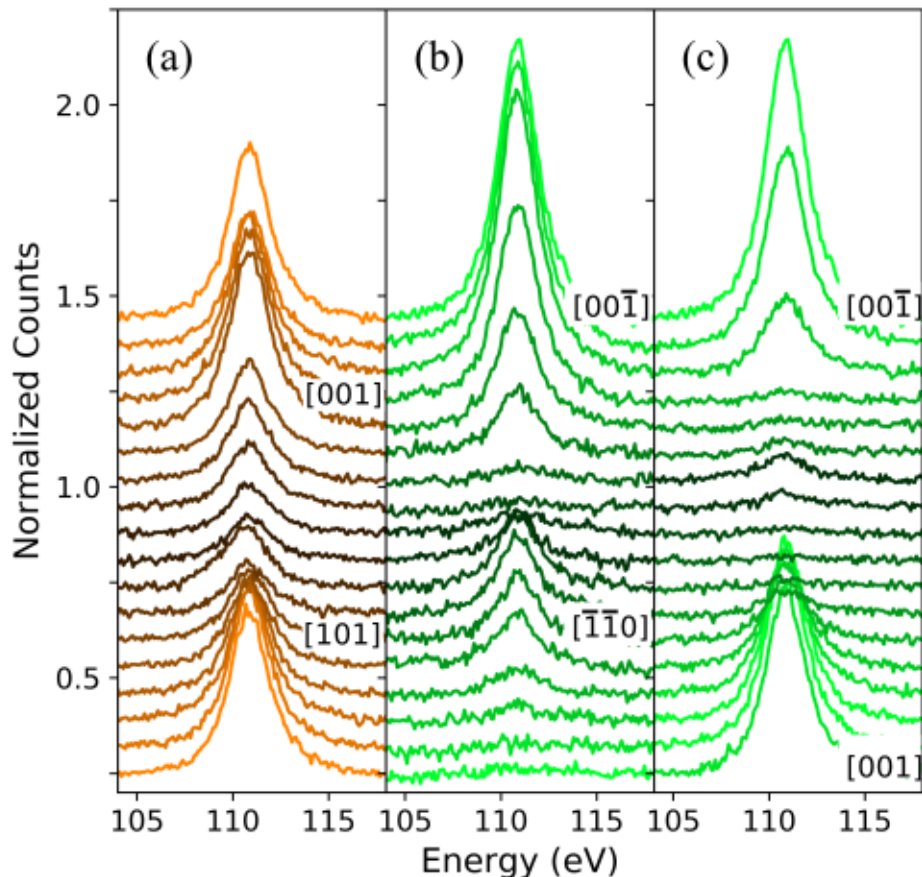


FIG. 3: Ni M_1 ($3s \rightarrow 3d$) edge spectra. A close-up view of the relevant range of the spectra after background subtraction and normalization. Panel (a) shows data for momentum transfer vector \vec{q} sweeping on a plane defined by $\vec{q}||[001]$ and $\vec{q}||[100]$ and (b-c) on a plane defined by $\vec{q}||[001]$ and $\vec{q}||[110]$. Spectra corresponding to major axes are marked accordingly, and the spectra in between are plotted sequentially. Panel (b) shows the spectra, where \vec{q} is sweeping clockwise from $\vec{q}||[001]$, passing $\vec{q}||[\bar{1}\bar{1}0]$, and ending where the projection of the orbital function vanishes. Similarly, panel (c) shows data, where \vec{q} is sweeping counterclockwise from $\vec{q}||[00\bar{1}]$ towards $\vec{q}||[001]$. The data are vertically shifted for clarity. The scattering intensity of the M_1 edge excitations ($3s \rightarrow 3d$) depends strongly on the relative orientation of momentum transfer and crystallographic direction in the NiO single crystal.

orbital shapes in Fig. 4 (b): the blue dashed line is the $3d(x^2 - y^2)3d(3z^2 - r^2)$ function and the solid line is the same function convoluted with the angular acceptance of the 3×4 analyzers we used in our experiment (see Methods in Section Supplementary). The near perfect agreement further demonstrates the accuracy of the method.

The directional dependence of the integrated s -NIXS intensity at the Ni M_1 edge ($3s \rightarrow 3d$) directly maps the local orbital hole of the ion in the ground state. There is no need to carry out multiplet analysis of the spectral line shape to extract this information, in contrast to, for example, the non- s edges (e.g. $L_{2,3}(2p)$, $M_{2,3}(3p)$, $M_{4,5}(3d)$, $N_{4,5}(4d)$, and $O_{4,5}(5d)$) in both NIXS [7–13, 16, 22, 23] and XAS experiments [17–21]. The reason is fundamental: The M_1 ($3s \rightarrow 3d$) quadrupolar excitation process involves a spherically symmetric s orbital, so the angular distribution of intensity is solely deter-

mined by the hole charge distribution in the initial state with respect to the momentum transfer \vec{q} . This is similar to the dipole-allowed $s \rightarrow p$ transition in XAS, where an angular sweep of the polarization dependence maps out the orientation of the p hole directly. We would like to emphasize that details of the s -NIXS final states do not matter because the information is extracted from the integrated intensity of the spectra (i.e. from the sum of the intensities of all final states). As a result, only the properties of the initial state are probed. This is analogous to using spectral sum rules to extract expectation values of the relevant quantum numbers of the system in the ground state [20, 25, 26]. The power of s -NIXS, as compared to XAS, is that it allows transitions not only from s -to- p , but also from s -to- d and s -to- f due to the possibility of going beyond the dipole limit when using large momentum transfers $|\vec{q}|$.

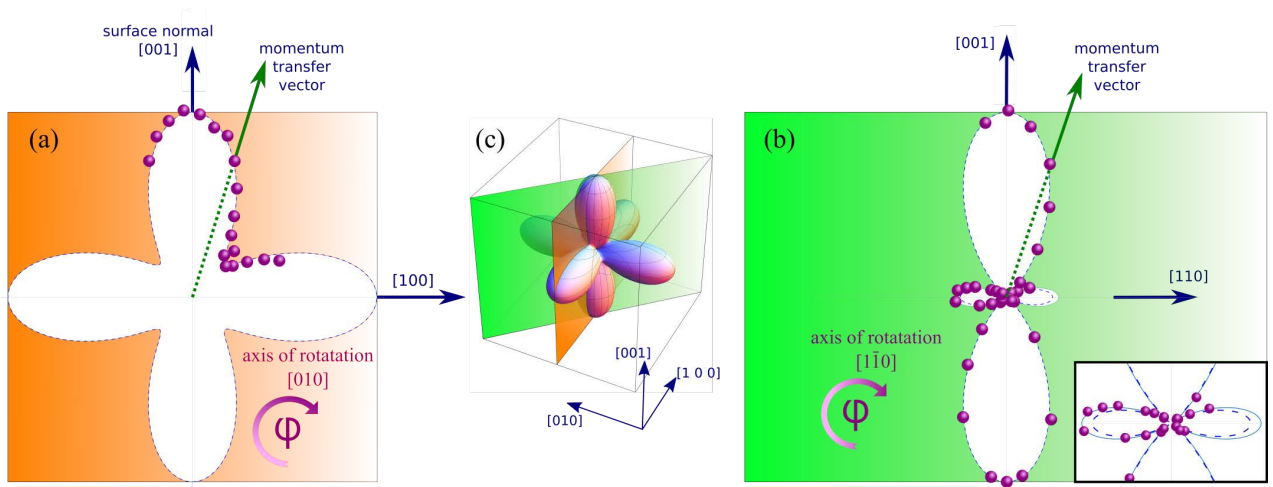


FIG. 4: Orbital shape of ${}^3A_2 3d(x^2 - y^2)3d(3z^2 - r^2)$ hole density. Three-dimensional hole density distribution of the Ni high-spin $3d^8$ configuration (c). Projection of the three-dimensional orbital shape on two planes defined by (a) [001] and [100] and (b) [001] and [110]. Data points on polar plots (a-b) are integrated intensities for Ni M_1 ($3s \rightarrow 3d$) for corresponding φ , which is the angle between the momentum transfer vector \vec{q} and the surface normal vector [001] for both cases (a-b). For (a) the sample is rotated such that the \vec{q} sweeps between [001] and [100], and for (b) \vec{q} sweeps between [001] and [110]. Inset in (b) demonstrates the theoretical orbital function (blue dashed line) and the corrected function as a result of an angular convolution with the 3×4 analyzer array. For (a), the correction was insignificant.

The s -NIXS process involves a core hole, meaning that both the electronic structure of the system and consequently the measured valence hole are projected locally. The intensity distribution is not what would be measured in an x-ray diffraction (XRD) experiment, even if such an experiment could be carried out with sufficient accuracy. In fact, it would be extremely difficult for transition metal, rare earth, and actinide compounds to be measured with the desired accuracy in XRD due to their relatively small number of valence electrons with respect to core electrons. s -NIXS provides information complementary to that from an XRD experiment by elucidating which local orbital or atomic wave function is active.

The s -NIXS method presented here is not limited to ionic materials. In cases where configuration interaction effects play an important role due to covalency or itinerancy, the image of the probed local orbital will reflect these effects directly. The strength of s -core-level NIXS is that the information is extracted from the \vec{q} -directional dependence of the *integrated* intensity and not from the *line shape* of the spectra. Thus, the details of the final states are no longer important, rendering complex configuration interaction calculations unnecessary. The sole \vec{q} -directional dependence is rooted in the spherical symmetry of the s -core hole.

To conclude, we have directly imaged one of the fundamental quantum mechanical objects in crystals, namely, a d -orbital, which is derived purely mathematically from first principles. We have revealed that non-resonant inelastic x-ray scattering involving an s -core level is an extremely powerful and accurate experimental method to

determine the local orbital in the ground state. Albeit low cross-section, the excellent signal to background ratio allows for highly reliable results. The procedure relies on the integrated intensity of the signal, which tremendously simplifies the interpretation as there is no need to carry out multiplet analysis of the spectral line shape to extract the desired information. The method is element specific, which is invaluable for unraveling the different origins for electron correlation effects in complex materials. Since the probing photons have high penetrating power, the measurements are bulk sensitive, and can be performed with complex sample environments (e.g. small samples, high pressures, high/low temperatures). We believe that this method opens up new opportunities for the study of a wide range of d and f electron containing materials, where knowledge of their local wave function is of central importance to reveal their underlying physics and thus provide guidance for the design of new quantum materials.

ACKNOWLEDGMENT

M.S., K.C., A.A. and A.S. gratefully acknowledge support from the German funding agency DFG under Grant No SE1441-4-1.

APPENDIX

Experiment:

Non-resonant inelastic x-ray scattering (NIXS) measurements were performed at the High-Resolution Dynamics Beamline P01 of PETRA-III synchrotron in Hamburg, Germany. Fig. 1 illustrates the experimental setup, showing the incoming beam (\vec{k}_i, ω_i), sample, scattered beam (\vec{k}_f, ω_f), and the corresponding momentum transfer vector (\vec{q}). The energy of the x-ray photon beam incident on the sample was tuned with a Si(311) double-reflection crystal monochromator (DCM). The photons scattered from the sample were collected and energy-analyzed by an array of twelve spherically bent Si(660) crystal analyzers. The analyzers are arranged in a 3x4 configuration. The energy of the analyzers ($\hbar\omega_f$) was fixed at 9690 eV; the energy loss spectra were measured by scanning the energy of the DCM ($\hbar\omega_i$). Each analyzer signal was individually recorded by a position-sensitive custom-made LAMBDA detector. The energy calibration was regularly checked by measuring the zero-energy-loss position of each spectrum. The best possible energy resolution was guaranteed by pixel-wise analysis of the detector recordings and measured as 0.7 eV (FWHM).

The positioning of the analyzer array determines the momentum transfer vector and the corresponding scattering triangle, which is defined by the incident and scattered photon momentum vectors, \vec{k}_i and \vec{k}_f , respectively. The large scattering angle ($2\theta \approx 155^\circ$) chosen for the current study assured a large momentum transfer of $|\vec{q}| = (9.6 \pm 0.1) \text{ \AA}^{-1}$ when averaged over all analyzers. \vec{k}_f and 2θ were kept constant by fixing the energy and the position of the analyzer array. Since the energy transfer range of interest (100 to 120 eV) was small with respect to the incident and final energies (~ 9700 eV), variation of \vec{k}_i during energy scanning was insignificant. This guaranteed that the scattering triangle was virtually unchanged throughout the course of the experiment with $|\vec{q}| \approx \text{constant}$.

Sample

NiO single crystal (SurfaceNet, Germany) was kept at $T = 20\text{K}$ throughout the experiment. It was aligned as in Fig. 1 and rotated by angle φ around an axis perpendicular to the [010] lattice direction; $\vec{q} \parallel [001]$ ($\varphi = 0$) corresponds to specular geometry. Energy scans were taken for many values of φ so that the directional dependence of $S(\vec{q}, \omega)$ could be measured for \vec{q} sweeping between $\vec{q} \parallel [001]$ and $\vec{q} \parallel [100]$. For the second set of measurements, the crystal was reoriented to evaluate $S(\vec{q}, \omega)$ on the $\vec{q} \parallel [001]$ - $\vec{q} \parallel [110]$. This time, the axis of rotation was along $[110]$.

Data Treatment

The data were normalized to the Compton peak at about 350 eV energy transfer (see Fig. 2). Subsequently, a linear background was subtracted from each spectrum in order to account for the Compton scattering in the energy range of the Ni M_1 edge.

Since the analyzer array (3x4) is spread over a finite solid angle, each measured spectrum $S(\vec{q}, \omega)$ includes an array of momentum transfer vectors \vec{q} corresponding to individual analyzers. In this case, taking an average \vec{q} does not work for directions where the orbital wave function varies significantly for small angular changes (i.e. small lobes of the $3d(3z^2 - r^2)$). The theoretical orbital wave function should be convoluted with the angular spread of the analyzer array to reflect this effect. The inset on Fig. 4 (b) demonstrates the theoretical function (blue dashed line) and the convoluted function (solid line), which agrees well with the data points.

* Present address: SLAC National Accelerator Lab., 2575 Sand Hill Rd, Menlo Park, CA 94025, USA

† present address: Synchrotron SOLEIL, L'Orme des Merisiers, Saint-Aubin, BP 48, 91192 Gif-sur-Yvette Cedex, France

- [1] R. J. Cava, *Journal of the American Ceramic Society* **83**, 5 (2008).
- [2] D. I. Khomskii, *Transition Metal Compounds* (Cambridge University Press, 2014).
- [3] B. Keimer, S. A. Kivelson, M. R. Norman, S. Uchida, and J. Zaanen, *Nature* **518**, 179 (2015).
- [4] S. Wirth and F. Steglich, *Nature Reviews Materials* **1**, 16066 (2016).
- [5] C. Pfeleiderer, *Rev. Mod. Phys.* **81**, 1551 (2009).
- [6] G. R. Fowles, *Introduction to Modern Optics* (Holt, Rinehart and Winston, Inc., 1968).
- [7] W. Schülke, *Electron dynamics by Inelastic x-ray scattering* (Oxford University Press, 2008).
- [8] M. W. Haverkort, A. Tanaka, L. H. Tjeng, and G. A. Sawatzky, *Phys. Rev. Lett.* **99**, 257401 (2007).
- [9] R. A. Gordon, G. T. Seidler, T. T. Fister, M. W. Haverkort, G. A. Sawatzky, A. Tanaka, and T. K. Sham, *EPL (Europhysics Letters)* **81**, 26004 (2008).
- [10] R. A. Gordon, M. W. Haverkort, S. SenGupta, and G. A. Sawatzky, *J. Phys. Conf. Ser.* **190**, 012047 (2009).
- [11] J. A. Bradley, S. Sen Gupta, G. T. Seidler, K. T. Moore, M. W. Haverkort, G. A. Sawatzky, S. D. Conradson, D. L. Clark, S. A. Kozimor, and K. S. Boland, *Phys. Rev. B* **81**, 193104 (2010).
- [12] R. Caciuffo, G. van der Laan, L. Simonelli, T. Vitova, C. Mazzoli, M. A. Denecke, and G. H. Lander, *Phys. Rev. B* **81**, 195104 (2010).
- [13] J. A. Bradley, K. T. Moore, G. van der Laan, J. P. Bradley, and R. A. Gordon, *Phys. Rev. B* **84**, 205105 (2011).
- [14] G. van der Laan, *Phys. Rev. Lett.* **108**, 077401 (2012).
- [15] G. van der Laan, *Phys. Rev. B* **86**, 035138 (2012).

- [16] T. Willers, F. Strigari, N. Hiraoka, Y. Q. Cai, M. W. Haverkort, K.-D. Tsuei, Y. F. Liao, S. Seiro, C. Geibel, F. Steglich, et al., *Phys. Rev. Lett.* **109**, 046401 (2012).
- [17] C. T. Chen, L. H. Tjeng, J. Kwo, H. L. Kao, P. Rudolf, F. Sette, and R. M. Fleming, *Phys. Rev. Lett.* **68**, 2543 (1992).
- [18] F. de Groot, *J. Electron Spectros.* **67**, 529 (1994), ISSN 0368-2048.
- [19] A. Tanaka and T. Jo, *J. Phys. Soc. Jpn.* **63**, 2788 (1994).
- [20] S. I. Csiszar, M. W. Haverkort, Z. Hu, A. Tanaka, H. H. Hsieh, H.-J. Lin, C. T. Chen, T. Hibma, and L. H. Tjeng, *Phys. Rev. Lett.* **95**, 187205 (2005).
- [21] P. Hansmann, A. Severing, Z. Hu, M. W. Haverkort, C. F. Chang, S. Klein, A. Tanaka, H. H. Hsieh, H.-J. Lin, C. T. Chen, et al., *Phys. Rev. Lett.* **100**, 066405 (2008).
- [22] M. Sundermann, M. W. Haverkort, S. Agrestini, A. Al-Zein, M. M. Sala, Y. Huang, M. Golden, A. de Visser, P. Thalmeier, L. H. Tjeng, et al., *Proc. Nat. Acad. Science. U.S.A.* **113**, 13989 (2016).
- [23] M. Sundermann, H. Yavaş, K. Chen, D. J. Kim, Z. Fisk, D. Kasinathan, M. W. Haverkort, P. Thalmeier, A. Severing, and L. H. Tjeng, *Phys. Rev. Lett.* **120**, 016402 (2018).
- [24] G. A. Sawatzky and J. W. Allen, *Phys. Rev. Lett.* **53**, 2339 (1984).
- [25] B. T. Thole, P. Carra, F. Sette, and G. van der Laan, *Phys. Rev. Lett.* **68**, 1943 (1992).
- [26] P. Carra, B. T. Thole, M. Altarelli, and X. Wang, *Phys. Rev. Lett.* **70**, 694 (1993).